Time-resolved turbulent dynamo in a laser plasma

Archie F. A. Bott[a,b,1], Petros Tzeferacos[a,c,d,e], Laura Chen[a], Charlotte A.J. Palmer[a,f], Alexandra Rigby[a], Anthony R. Bell[a], Robert Bingham[g,h], Andrew Birkel[i], Carlo Graziani[j], Dustin H. Froula[e], Joseph Katz[e], Michel Koenig[k,l], Matthew W. Kunz[b], Chikang Li[i], Jena Meinecke[a], Francesco Miniati[a], Richard Petrasso[i], Hye-Sook Park[m], Bruce A. Remington[m], Brian Reville[n], J. Steven Ross[m], Dongsu Ryu[o], Dmitri Ryutov[m], Fredrick Séguin[i], Thomas G. White[p], Alexander A. Schekochihin[a], Donald Q. Lamb[c], and Gianluca Gregori[a,c]

[a]Department of Physics, University of Oxford, Parks Road, Oxford OX1 3PU, UK; [b]Department of Astrophysical Sciences, Princeton University, 4 Ivy Ln, Princeton, NJ 08544, USA; [c]Department of Astronomy and Astrophysics, University of Chicago, 5640 S. Ellis Ave, Chicago, IL 60637, USA; [d]Department of Physics and Astronomy, University of Rochester, 206 Bausch & Lomb Hall, Rochester, NY 14627; [e]Laboratory for Laser Energetics, University of Rochester, 250 E River Rd, Rochester, NY 14623, USA; [f]School of Mathematics and Physics, Queens University Belfast, Belfast BT7 1NN, UK; [g]Rutherford Appleton Laboratory, Chilton, Didcot OX11 0QX, UK; [h]Department of Physics, University of Strathclyde, Glasgow G4 0NG, UK; [i]Massachusetts Institute of Technology, 77 Massachusetts Ave, Cambridge, MA 02139, USA; [j]Argonne National Laboratory,Mathematics and Computer Science Division, Argonne, IL, USA; [k]LULI, CNRS, CEA, Ecole Polytechnique, UPMC, Univ Paris 06: Sorbonne Universites, Institut Polytechnique de Paris, F-91128 Palaiseau cedex, France; [l]Graduate School of Engineering, Osaka University, Suita, Osaka 565-0871, Japan; [m]Lawrence Livermore National Laboratory, 7000 East Ave, Livermore, CA 94550, USA; [n]Max-Planck-Institut für Kernphysik, Postfach 10 39 80, 69029 Heidelberg, Germany; [o]Department of Physics, School of Natural Sciences, UNIST, Ulsan 44919, Korea; [p]Department of Physics, University of Nevada, Reno, Nevada 89557, USA

This manuscript was compiled on February 1, 2021

Understanding magnetic-field generation and amplification in turbulent plasma is essential to account for observations of magnetic fields in the universe. A theoretical framework attributing the origin and sustainment of these fields to the so-called fluctuation dynamo was recently validated by experiments on laser facilities in low-magnetic-Prandtl-number plasmas ($\mathrm{Pm} < 1$). However, the same framework proposes that the fluctuation dynamo should operate differently when $\mathrm{Pm} \gtrsim 1$, the regime relevant to many astrophysical environments such as the intracluster medium of galaxy clusters. This paper reports a new experiment that creates a laboratory $\mathrm{Pm} \gtrsim 1$ plasma dynamo for the first time. We provide a time-resolved characterization of the plasma's evolution, measuring temperatures, densities, flow velocities and magnetic fields, which allows us to explore various stages of the fluctuation dynamo's operation on seed magnetic fields generated by the action of the Biermann-battery mechanism during the initial drive-laser target interaction. The magnetic energy in structures with characteristic scales close to the driving scale of the stochastic motions is found to increase by almost three orders of magnitude and saturate dynamically. It is shown that the initial growth of these fields occurs at a much greater rate than the turnover rate of the driving-scale stochastic motions. Our results point to the possibility that plasma turbulence produced by strong shear can generate fields more efficiently at the driving scale than anticipated by idealized MHD simulations of the nonhelical fluctuation dynamo; this finding could help explain the large-scale fields inferred from observations of astrophysical systems.

Magnetic fields | Fluctuation dynamo | Laboratory astrophysics |

Cosmic magnetic fields play a dynamically important role in a myriad of astrophysical environments (1, 2). Understanding how these fields attained such strengths is a long-standing question in astrophysics (3). Most physical processes thought to generate seed magnetic fields in initially unmagnetized plasma, such as the Biermann battery mechanism (4), predict field-strength values in astrophysical settings that are far smaller than those observed (5, 6), necessitating the existence of some mechanism for amplifying fields and maintaining them at their observed magnitudes (7, 8). One possible mechanism is the fluctuation dynamo, whereby stochastic motions of plasma lead to stretching, twisting and folding of magnetic-field lines (9, 10). In this dynamo, fields are amplified exponentially until their strength comes into approximate equipartition with the fluid kinetic energy, saturating growth.

The fluctuation dynamo is best understood in the context of resistive magnetohydrodynamics (MHD) thanks to both analytical calculations (11–14) and simulations (15–25). In resistive MHD, the fluctuation dynamo can only operate if the magnetic Reynolds number $\mathrm{Rm} \equiv u_L L/\eta$ – where L is the length scale of driving stochastic motions, u_ℓ the characteristic velocity of motions at a given scale ℓ, and η the resistivity of the plasma – is above some critical threshold, $\mathrm{Rm_c}$ (26). The precise value of this threshold depends on the magnetic Prandtl number Pm of the plasma (21, 27, 28), defined by $\mathrm{Pm} \equiv \mathrm{Rm}/\mathrm{Re} = \nu/\eta$ (where $\mathrm{Re} \equiv u_L L/\nu$ is the fluid Reynolds number and ν is the kinematic viscosity), as well as the Mach number and driving mechanism of the stochastic motions (29). If this threshold is surpassed, then any initially dynamically insignificant magnetic field is amplified, and most rapidly so near the resistive scale $\ell_\eta \ll L$ (for $\mathrm{Pm} \ll 1$, $\ell_\eta \sim \eta/u_{\ell_\eta}$; for

Significance Statement

Our laser-plasma experiment has reproduced the physical process thought to be responsible for generating and sustaining magnetic fields in turbulent plasmas (the 'fluctuation dynamo'), and, for the first time in the laboratory, has accessed the viscosity-dominated regime of relevance to most of the plasma in the universe. Also for the first time, these measurements are time-resolved, which provides evolutionary information about the fluctuation dynamo (including the field's growth rate) previously only available from simulations. The efficient amplification of large-scale magnetic fields seen in our experiment could explain the origin of large-scale fields that are observed in turbulent astrophysical plasmas, but are not predicted by current analytical calculations or idealized simulations of the fluctuation dynamo.

This project was conceived by G.G., D.Q.L., P.T., A.F.A.B., and A.A.S.. The delivery of the experiment was led by G.G. and L.C.. A.B., C.-K.L. and R.P. contributed to the proton radiography development and data extraction, while D.H.F. and J.K. contributed to the Thomson scattering diagnostics. P.T. designed, executed, and analyzed the FLASH simulations. The analysis of the experimental and simulation data was led by A.F.A.B. with support from P.T., L.C., C.P., A.R., A.R.B., R.B., A.B., C.G., J.K., M.K., C.-K.L., J.M., J.M., R.P., H.-S.P.,B.A.R., B.R., J.S.R., D.Ryu, D.Ryutov, T.G.W., A.A.S., D.Q.L., and G.G. The paper was written by A.F.A.B. with contributions from all other co-authors.

A.F.A.B., M.W.K., and N.B. are affiliated with Princeton University. They have not collaborated. The authors declare that they have no other conflicts of interest.

[1]To whom correspondence should be addressed. E-mail: abott@princeton.edu

$\mathrm{Pm} \gtrsim 1$, $\ell_\eta \sim \eta/u_{\ell_\nu}$). The nature of this amplification depends on Pm, because Pm determines the relative magnitudes of ℓ_η and the viscous scale $\ell_\nu \sim \nu/u_{\ell_\nu}$, and thereby whether the stochastic fluid motions driving dynamo action are smooth or chaotic (27). The $\mathrm{Pm} \ll 1$ regime is relevant to stellar and planetary dynamos, while the $\mathrm{Pm} \gtrsim 1$ regime is pertinent to hot, diffuse plasmas such as many astrophysical disks or the intracluster medium (ICM) (10).

A fundamental question about the character of the fluctuation dynamo in resistive MHD concerns the rate of magnetic-field growth at a given scale. When the growing field is dynamically insignificant, its spectrum is peaked near the resistive scale (11, 14); magnetic fluctuations at this scale grow exponentially, at a rate proportional to the characteristic turnover rate $\gamma_{\ell_\nu} \sim u_{\ell_\nu}/\ell_\nu$ of motions at the viscous scale (for $\mathrm{Pm} \gtrsim 1$). For Kolmogorov turbulence, γ_{ℓ_ν} greatly exceeds the characteristic turnover rate $\gamma_L \sim u_L/L$ of the driving-scale stochastic motions. Once the magnetic energy at resistive scales becomes comparable to the kinetic energy at the viscous scale, MHD simulations indicate that the magnetic-energy spectrum changes, with the total energy continuing to grow – albeit secularly rather than exponentially – and the peak wavenumber moving to scales larger than the resistive scale (19, 23, 30). Whether the peak wavenumber ultimately moves to the driving scale of the motions depends on Pm: previous simulations of the $\mathrm{Pm} \sim 1$ dynamo (with non-helical flow) suggest that in the saturated state of the dynamo the peak wavenumber is a factor of a few larger than the driving wavenumber (22, 31), while for $\mathrm{Pm} \gg 1$, an excess of energy remains near the resistive scale (19). Thus, whilst simulations of the fluctuation dynamo show that magnetic fields can be amplified very quickly at the resistive scale, dynamically significant fields on the driving scales only develop after many driving-scale eddy turnover times, or possibly not at all.

With dynamo experiments now possible, we have a method for exploring both the requirements for, and the properties of, the fluctuation dynamo. Until recently, experimental investigations of plasma dynamos were limited by the practical difficulty of realizing sufficiently large values of Rm in the laboratory (32–35). However, a recent laser-plasma experiment (36, 37) carried out on the Omega Laser Facility (38) demonstrated the feasibility of the fluctuation dynamo in a turbulent plasma at $\mathrm{Pm} < 0.5$. In that experiment, a region of turbulent plasma was created by colliding two laser-plasma jets that had first passed through offset grids. The state of this region was characterized, and the magnetic Reynolds number $\mathrm{Rm} \approx 600$ was above the necessary threshold for the onset of the fluctuation dynamo in MHD. Magnetic fields were measured using both polarimetry and proton imaging, and the magnetic-energy density in the turbulent plasma a few turnover times after collision was found to be several orders of magnitude larger than that present during the turbulent region's formation. Most significantly, this magnetic-energy density was a finite fraction of the turbulent kinetic-energy density, a key signature of the saturated fluctuation dynamo.

In this paper, we report new experiments on the Omega Laser Facility, which employs a re-designed version of the platform described in (37) to create the first laboratory $\mathrm{Pm} \gtrsim 1$ fluctuation dynamo. As before, we used three-dimensional radiation-MHD simulations with FLASH (39, 40) to design and interpret the experiments – see Supplementary Information for details. Also for the first time, by carrying out multiple identical experiments, we are able to provide a time-resolved characterization of this plasma dynamo's evolution by measuring spatially averaged electron and ion temperatures, densities, flow velocities, and magnetic fields with a time resolution smaller than the turnover time of the plasma's driving-scale stochastic motions. Such a characterization is an important advance over our previous OMEGA experiment, which did not measure the growth rate of magnetic fields. Finally, the concerted analysis of the experimental data in tandem with the simulation results enabled a thorough assessment of the dynamo mechanism realized in our experiment.

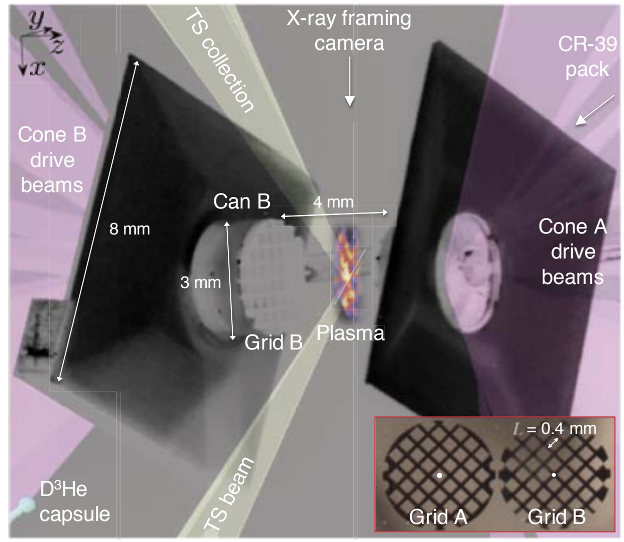

Fig. 1. Experimental set-up. An annotated photograph of a target used in our experiment. The laser-beam-driven foils are composed of CH plastic (i.e., 50% carbon, 50% hydrogen by atom number) and are 3 mm in diameter and 50 μm in thickness; attached to the front sides of each foil are 230 μm thick, 3 mm diameter annular 'washers', also composed of CH plastic, with a 400 μm central hole. The separation between the two opposing foils is 8 mm. The shields (which prevent direct interaction between the front- and rear-side blow-off plasmas) are also CH plastic. CH plastic cans attach polyimide grids to the foils; the grids themselves are 250 μm thick, with a 3 mm diameter, 300 μm holes and 100 μm wires. The holes in the opposing grids are chosen to be offset (see bottom right); grid A has a hole located at its center, while grid B has crossing rods. Ten 500 J drive beams (individual pulse length 1 ns) with 351 nm wavelength and 800 μm focal spot size were applied to each foil, configured to deliver a 10 ns staggered flat pulse shape with a total energy per foil of 5 kJ. The orientation of the Thomson scattering (TS) beam is denoted, as well as the cylindrical scattering volume and collection direction. A D^{3}He capsule is attached to the target for the proton imaging diagnostic (see Materials and Methods for details): fusion protons are generated by the capsule's implosion, pass between the target grids, and are detected via a CR-39 pack positioned as shown. For ease of reference between figures, we have defined an (x, y, z) Cartesian coordinate system with axes as shown, whose origin is at the target's center.

Experimental Design

The experimental platform employed for the experiment (see Fig. 1 for a schematic of the experimental target) generates a turbulent plasma in the following manner. Ten long-pulse laser beams illuminate two opposing CH foils, creating counter-propagating supersonic plasma jets. These jets then pass through offset grids before colliding at the experimental target's center. On collision, the jets coalesce, forming an 'interaction region' of plasma (demarcated by two shocks) whose density and temperature are significantly greater than that of either jet. The inhomogeneity and asymmetry of the initial plasma-jet density and flow profiles gives rise to significant shearing motions in the interaction region; this facilitates Kelvin-Helmholtz (KH) instabilities over a range of length scales, and thus significant stochasticity emerges in the flow profile as the interaction region develops. In contrast to the initial jet motion, stochastic motions in the interaction region are subsonic, because of their reduced characteristic speeds and the higher temperature of the plasma in the interaction-region (a result of compressive heating). At a given instant, we characterize this plasma using various experimental diagnostics: X-ray imaging for investigating the spatial distribution of the plasma in the interaction region plasma (see Section A), optical Thomson scattering for measuring the plasma properties (Section B), and proton imaging for quantifying magnetic fields (Section C).

Despite some similarities with the previous OMEGA experiment investigating dynamo processes (37), the design of the new experiment was different in a key regard. In order to realize a larger Pm, chlorine dopants previously introduced into the CH foils to enhance X-ray emissivity of the plasma were removed. Their presence in even moderate quantities was found to reduce initial plasma-jet velocities, cool the plasma radiatively and increase the effective ion charge; all three effects in combination reduced Pm significantly. We also made a number of other improvements to the target's design. The thickness of the grid wires was decreased to 100 μm, whilst the hole width was kept at 300 μm (see Fig. 1, bottom right). This change was made in order to deliver more kinetic energy to the interaction region and reduce the inhomogeneity of the interaction region's global morphology arising from the asymmetry of the grids. Finally, rod supports connecting the grids to the CH foils were removed and the grids instead attached via CH 'cans' (see Fig. 1). This alteration provided both the X-ray framing camera and proton imaging diagnostics with unobstructed views of the interaction region. Further discussion of these target modifications is given in (41).

We also changed somewhat our methodology for diagnosing the plasma state. Instead of employing the Thomson-scattering diagnostic to measure polarization [as was done in (37)], we used it to measure the spectra of high-frequency fluctuations [the electron-plasma-wave (EPW) feature] as well as low-frequency fluctuations [the ion-acoustic-wave (IAW) feature] concurrently. Furthermore, instead of the previous setup that measured the scattering spectrum in a small volume during a 1-ns time window, we employed a spatially resolved, 1-ns time-integrated set-up that measured the plasma parameters in a cylindrical region passing through the grids' midpoint, with length 1.5 mm and a 50 μm^2 cross-sectional area (see Fig. 1). This enabled us to measure simultaneously the values of a number of plasma parameters characterizing the interaction-region plasma: mean electron number density $\bar{n}_e$, fluctuating electron number density Δn_e, electron temperature T_e, ion temperature T_i, inflow velocity $\bar{u}_{\rm in}$ and small-scale stochastic velocity Δu. Removing polarimetry from this experiment did not inhibit our ability to measure magnetic fields, because we had previously validated the accuracy of such measurements obtained using proton imaging (42).

In order to characterize the growth of the magnetic fields in our experiment with the requisite time resolution, we began to collect data prior to collision and continued to do so at 1.5-ns intervals (on different experimental shots). This time interval was correctly anticipated to be less than half of the turnover time of driving-scale eddies ($\sim$4 ns), based on FLASH simulations that were validated by our earlier experiment (36, 37). Detailed specifications of the X-ray framing camera diagnostic, the Thomson-scattering diagnostic and the proton-imaging diagnostic are given in Materials and Methods.

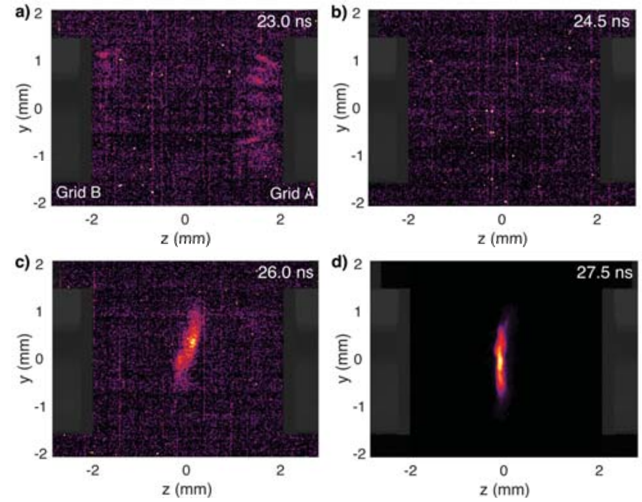

Fig. 2. X-ray self-emission prior to and at formation of the interaction region. The featured sequence of X-ray images are taken on different experimental shots. The first three images are adjusted to have the same color map, normalized to the maximum pixel count (56 counts) of c); the final image is normalized to its own maximum pixel count. We note that the absence of noise in d) is due to the much higher signal-to-noise ratio. To aid interpretation of the images, a projection of the target is superimposed in dark gray on each image. The respective timings (in ns) of the images after drive-beam laser-pulse initiation are **a)** 23.0 ns, **b)** 24.5 ns, **c)** 26.0 ns, and **d)** 27.5 ns.

Measurements

A. Measuring turbulence: self-emission X-ray imaging. With the fixed X-ray framing camera's bias employed in our experiment (see Materials and Methods), we find that for times $\lesssim 25$ ns, self-emitted X-rays from the individual plasma jets are barely detectable (see Fig. 2a and Fig. 2b). However, around 26 ns after the onset of the driving laser pulses, a region of emission situated approximately halfway between the grids emerges (Fig. 2c). 1.5 ns later, the total intensity of the region is significantly higher (Fig. 2d). We conclude that the two plasma flows collide and form the interaction region at around 26 ns. Subsequent to the formation of the interaction region, the size of the region of bright emission increases both in the direction parallel to the 'line of centers' (that is, to the line connecting the midpoints of grid A and grid B) and perpendicular to it (see Fig. 3). Emission peaks 3 ns after the interaction-region's coalescence, before decaying away at later times (first column of Fig. 3). Random fluctuations in the detected X-ray intensity across the emitting region appear concurrently with the peak emission (second column, Fig. 3) and subsequently become clearly noticeable by eye.

In order to distinguish fluctuations in emission from global inhomogeneities in the total self-emission from the interaction-region plasma, we construct relative X-ray intensity maps based on experimentally derived mean emission profiles (a technical description of how these profiles are derived is given in

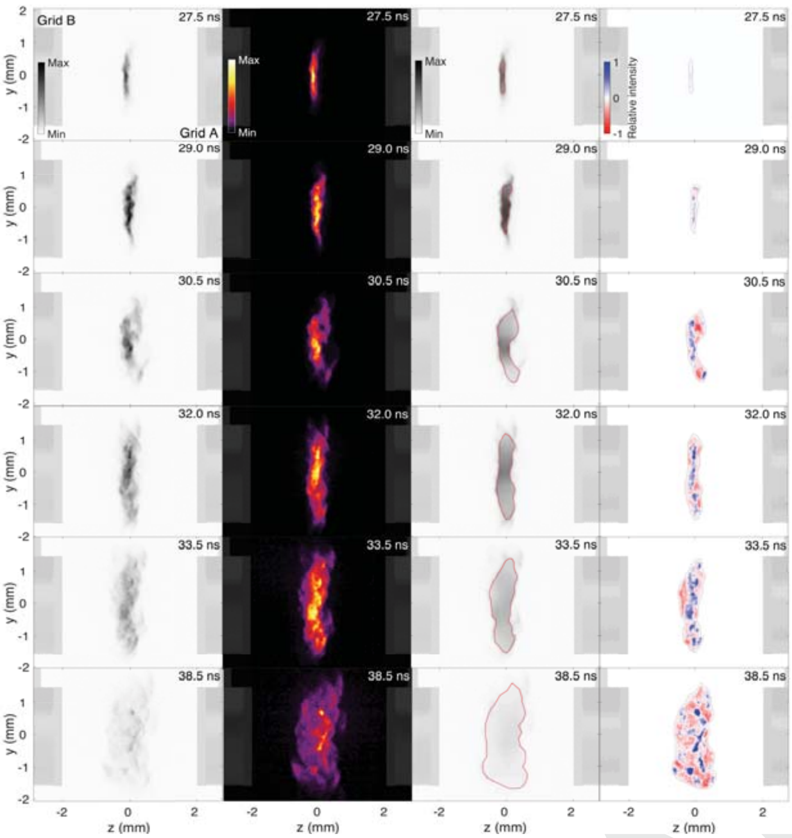

Fig. 3. The interaction-region plasma's evolution. Self-emission X-ray images of the interaction-region plasma. Each image was recorded at the indicated time in a different experimental shot. First column: absolute X-ray intensity images, normalized to a maximum count value of 1,050 (the maximum count value associated with the interaction-region plasma in any of the images). Second column: X-ray intensity images normalized by the maximum pixel value in the image. Third column: mean emission profiles calculated from the far-left column; the boundary denoted in red in each image is that used to calculate the two-dimensional (2D) Gaussian window function discussed in the main text and the gray-scale map is the same as in the far-left images. Fourth column: relative X-ray intensity map calculated from the mean emission profile. Fluctuations with a positive value with respect to the mean intensity are denoted in blue, negative in red, with maximum and minimum values set at $\pm 100\%$ of the mean value. Self-emission images for the FLASH simulations, as well as mean emission profiles and relative X-ray intensity maps associated with those images, are shown in Fig. S15 of the Supplementary Information.

the Supplementary Information). The mean emission profiles calculated for the X-ray images shown in the first column of Fig. 3 are given in the third column of the same figure and the corresponding relative-intensity images are presented in the fourth column.

Quantitative analysis of the X-ray images can be carried out by noting that the plasma jets are fully ionized even prior to collision ($T_e \approx 180\,\mathrm{eV}$), and so X-ray emission from the plasma during the interaction is dominated by free-free bremsstrahlung. Assuming a thermal distribution of particles, the bremsstrahlung spectral density $\epsilon_\omega^{\mathrm{ff}}$ for a CH plasma is given by (43)

$$\epsilon_\omega^{\mathrm{ff}} = 1.1 \times 10^{-38} Z_{\mathrm{eff}} n_e^2 T_e^{-1/2} \exp\left(-\frac{\hbar\omega}{k_B T_e}\right) \bar{g}_{\mathrm{ff}}\ \mathrm{erg\,cm^{-3}}, \quad [1]$$

where $Z_{\mathrm{eff}} = (Z_{\mathrm{C}}^2 + Z_{\mathrm{H}}^2)/(Z_{\mathrm{C}} + Z_{\mathrm{H}})$ is the effective ion charge seen by electrons (Z_{H} and Z_{C} being the charges of hydrogen and carbon ions, respectively), ω the frequency of radiation, k_B Boltzmann's constant, and $\bar{g}_{\mathrm{ff}}$ the velocity-averaged Gaunt factor. Since the interaction-region plasma is optically thin to X-rays detected by the framing camera, the measured (optical) intensity I on the CCD camera satisfies $I \propto \int \mathrm{d}s \int \mathrm{d}\omega\, \epsilon_\omega^{\mathrm{ff}} \hat{R}(\omega)$, where the integral is performed along the line of sight, and $\hat{R}(\omega)$ is a function incorporating the (relative) frequency-dependent responses of both the X-ray camera filter and the microchannel plate (MCP) (see Supplementary Information, Fig. S1). Substituting Eq. [1] into this proportionality relation, we find $I = I(n_e, T_e) \propto \int \mathrm{d}s\, n_e^2 \hat{f}(T_e)$, where

$$\hat{f}(T_e) = \frac{\hat{\mathcal{A}}}{T_e^{-1/2}} \int \mathrm{d}\omega\, \hat{R}(\omega) \exp\left(-\frac{\hbar\omega}{k_B T_e}\right), \quad [2]$$

and $\hat{\mathcal{A}}$ is a normalization constant. The function $\hat{f}(T_e)$ is plotted in the Supplementary Information (Fig. S1b); its key property is that for temperatures ~300–500 eV (the characteristic temperature of the plasma just after interaction-region formation – see Section B), the measured X-ray intensity is only weakly dependent on temperature. However, the X-ray intensity is a sensitive function of the electron number density: in short, our X-ray images essentially provide electron-density measurements.

This conclusion is significant for several reasons. First, the full-width-half-maximum (FWHM) of the emitting region can be used as a reasonable measure of the width l_n of the interaction region, on account of its increased density compared to either jet. Determining this width is essential for extracting magnetic-field estimates from the proton-imaging diagnostic (see Section C). Fig. 4a illustrates how this measurement is carried out in practice: we consider three vertically averaged lineouts of the mean emission profile, calculate the FWHMs of these lineouts, and then estimate the error of the measurement from the standard error of the FWHMs. The mean emission profile is marginally more robust than the original X-ray image for calculating l_n because fluctuations distort the measured maximum value of the vertically averaged profile. The resulting values of l_n are shown in Fig. 4c, in blue. Following an initial decrease in value immediately after the two plasma flows collide to form the interaction region, l_n increases steadily over time.

Secondly, relative fluctuations δI in X-ray intensity (such as those shown in Fig. 4b) are closely correlated with fluctuations δn_e of electron density; indeed, for intensity fluctuations that are small compared to the mean intensity $\bar{I}$, $\delta I/\bar{I} \approx 2/l_{n\perp} \int \mathrm{d}s\, \delta n_e/\bar{n}_e$, where $l_{n\perp}$ is the perpendicular extent of the interaction region (and we have assumed that $\delta T_e/\bar{T}_e \lesssim \delta n_e/\bar{n}_e$, which is justified by the small Péclet number of the interaction-region plasma: Pe ≈ 0.2). The root-mean-square (RMS) of the relative X-ray fluctuations therefore provides a simple measure of the onset of stochasticity in the interaction region. The increase in relative X-ray fluctuation magnitude $(\delta I/\bar{I})_{\mathrm{rms}}$ shown in Fig. 4c (in red) illustrates that significant fluctuations develop in a 5-ns interval following formation of the interaction region, after which their magnitude saturates at a finite fraction of the mean X-ray intensity of the region: $\delta I \lesssim 0.3\bar{I}$. Under the additional assumption that density fluctuations are statistically isotropic and homogeneous (see Fig. S16 for a justification of this), and therefore contribute to the line-of-sight integral as a random walk provided many fluctuations are sampled, we find $\delta n_e/\bar{n}_e \lesssim (l_{n\perp}/L_{\mathrm{int},n})^{1/2}\delta I/2\bar{I}$, where $L_{\mathrm{int},n}$ is the integral scale of the density fluctuations in the plasma. Taking $l_{n\perp} \lesssim 0.3$ cm and $L_{\mathrm{int},n} \approx L \approx 0.04$ cm (corresponding to the grid periodicity), we deduce that $\delta n_e/\bar{n}_e \lesssim 0.5$. Thus, it follows that density fluctuations are not large compared to the mean density and thus the stochastic motions of the plasma are subsonic.

Thirdly, under the same statistical assumptions, the power spectrum of the path-integrated density fluctuations derived from the X-ray intensity fluctuations can be directly related to the power spectrum of the density fluctuations (44). Because fluctuating density in a subsonic plasma behaves as a passive scalar (45), this in turn allows for the measurement of the velocity power spectrum (37). The result of such a calculation applied to Fig. 4b is shown in Fig. 4d: the spectrum extends across the full range of resolved wavenumbers and, for characteristic wavenumbers $2\pi/L \lesssim k < k_{\mathrm{res}} = 127\,\mathrm{mm}^{-1}$, the spectral slope is consistent with the Kolmogorov power law, as expected for a turbulent, subsonic plasma (46).

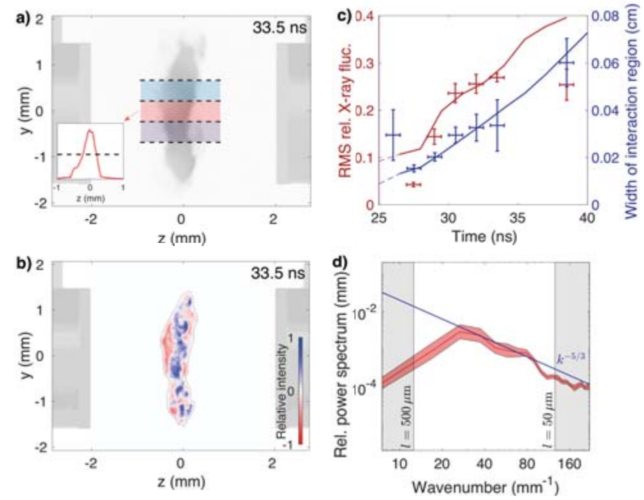

Fig. 4. Characterizing the interaction-region plasma using X-ray imaging. a) Mean emission profile of an X-ray image, recorded 33.5 ns after drive-beam pulse initiation, shown with regions used to calculate average one-dimensional (1D) parallel profiles. One such profile, along with the half-maximum value, is also depicted. **b)** Relative X-ray intensity map associated with mean emission profile given in a). **c)** Root-mean-square (RMS) of relative X-ray fluctuations (in red) and the width of the interaction region l_n over time (in blue). The behavior of both quantities in the FLASH simulations is also shown (red/blue curves). The dashed portion of the curves correspond to times when the interaction-region plasma is not yet fully collisional and so the simulations are not yet formally valid (see Supplementary Information). To determine an error of the RMS fluctuation measurement, the RMS values of fluctuations in images recorded at the same time are employed. **d)** 1D power spectrum of the relative density fluctuations (red line), calculated from the relative X-ray intensity map given in b). The error on the spectrum (pink patch) is determined using the power spectrum of b) and the power spectrum of the relative X-ray intensity map derived from the perturbed X-ray image at 33.5 ns equivalent to b) (cf. Fig. S7).

B. Measuring plasma parameters: Thomson-scattering diagnostic. For experimental times approximately coincidental with the collision of the two plasma flows, and just after, clear scattering spectra at both low and high frequencies were obtained. Unprocessed IAW and EPW features for a sample time close to the formation of the interaction region are shown in Figs. 5a and 5b, respectively; the complete data set used for these results is given in the Supplementary Information (Fig. S2). Measurements of the bulk plasma parameters listed in Experimental Design were then derived at a given position by fitting the spectral density function (see Materials and Methods). We averaged the parameters obtained from fits at each position over the complete spatial extent of the observed IAW and EPW features. The time evolution of the physical parameters was obtained by repeating the experiment and firing the Thomson-scattering diagnostic at different times with respect to the activation of the drive-beam.

The evolution of the average electron and ion temperatures in the Thomson-scattering volume is shown in Fig. 5c, density in Fig. 5d, and bulk and turbulent velocities in Fig. 5e. At 24 ns, the characteristic electron and ion temperatures were $T_e \approx T_i \approx 180\,\mathrm{eV}$, the characteristic flow speed $\bar{u}_{\mathrm{in}} \approx 260\,\mathrm{km\ s}^{-1}$, and the mean electron number density $\bar{n}_e \approx 2.5 \times 10^{19}\,\mathrm{cm}^{-3}$. These values are similar to those previously obtained for a single plasma jet (37), a finding consistent with the observation from the X-ray imaging diagnostic that the two plasma flows have not yet collided to form the interaction-region plasma at this time (see Fig. 2). By contrast, 1.5 ns later the electron and ion temperatures were found to be much larger than their jet pre-collision values: $T_e \approx T_i \approx 450\,\mathrm{eV}$. The measured mean electron number density also increased to $\bar{n}_e \approx 8 \times 10^{19}\,\mathrm{cm}^{-3}$. In fact, a range of densities were observed, with $\Delta n_e \approx 2 \times 10^{19}\,\mathrm{cm}^{-3}$, suggesting chaotic motions. For a measured characteristic sound speed of $c_s \approx 220\,\mathrm{km\ s}^{-1}$, this range of densities implies small-scale stochastic velocities $\Delta u \approx 55\,\mathrm{km\ s}^{-1}$ (see Materials and Methods). Assuming Kolmogorov scaling for the random small-scale motions – as is consistent with the spectrum in Fig. 4d – the characteristic velocity u_ℓ at scale ℓ satisfies $u_\ell \sim u_{\mathrm{rms}}(\ell/L)^{1/3}$. Because the dominant contribution to Δu arises from stochastic motions with scale comparable to the Thomson scattering cross-section width $l_{\mathrm{TS}} \approx 50\,\mu\mathrm{m}$, we conclude that $\Delta u \approx u_{l_{\mathrm{TS}}}$, and so $u_{\mathrm{rms}} \approx 110\,\mathrm{km\,s}^{-1}$.

In the 3-ns interval subsequent to the two plasma flows colliding to form the interaction region, the ion temperature increased above the electron temperature ($T_i \approx 600\,\mathrm{eV}$), before both fell to lower values ($T_e \approx T_i \approx 400\,\mathrm{eV}$). The mean electron number density increased monotonically over the same interval, with a final measured value of $\bar{n}_e \approx 1.8 \times 10^{20}\,\mathrm{cm}^{-3}$. The relative magnitude of density fluctuations remained the same ($\Delta n_e/\bar{n}_e \approx 0.25$) over the interval.

At later times, no EPW feature was observed and the IAW feature manifested itself erratically (see Fig. S3 in the Supplementary Information). We believe that this was due to the increased density of the interaction region (as well as substantial density gradients) resulting in significant refraction

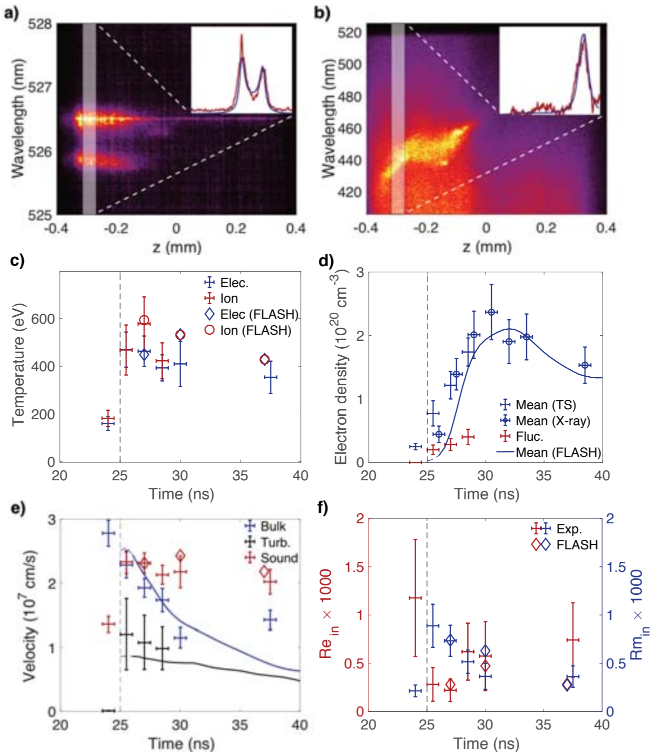

Fig. 5. Time-evolution of interaction-region plasma parameters. a) Low-frequency, spatially resolved spectrum (IAW feature) obtained at 27.2 ns. A sample spectral fit (for the white highlighted region) is shown in the inset. **b)** High-frequency, spatially resolved spectrum (EPW feature) and spectral fit (inset) obtained on the same shot. **c)** Evolution of electron and ion temperatures over time in the Thomson scattering volume. The experimental values for the electron (blue) and ion (red) temperatures are shown as time intervals with vertical error bars. All values are determined as described in the main text; errors for each time are determined by regarding each spatially resolved measurement as a sample of the mean temperature value for the interaction region, with the uncertainty on each sample determined by the fit sensitivity. The results of the FLASH simulations (see the Supplementary Material) for the electron temperature are shown as blue diamonds, those for the ion temperature as red circles. **d)** Evolution of mean electron density $\bar{n}_e$ (blue) and the fluctuating density Δn_e (red) with time in the interaction region. Also shown are experimental values of $\bar{n}_e$ derived from the self-emission X-ray images (open blue circles). The error bars are calculated in the same manner as for the temperature. The blue curve shows the results of the FLASH simulations. **e)** Evolution of bulk flow speed $\bar{u}_{\rm in}$ (blue), sound speed c_s (red) and turbulent velocity $u_{\rm rms}$ (black) with time in the Thomson-scattering volume. Errors are calculated in the same way as those for the temperature. Also shown are the results of the FLASH simulations for the bulk flow speed (blue curve), turbulent velocity (black curve), and sound speed (red diamonds). **f)** Evolution of the (bulk) fluid Reynolds number $\mathrm{Re_{in}} \equiv \bar{u}_{\rm in} L/\nu$ (red) and magnetic Reynolds number $\mathrm{Rm_{in}} \equiv \bar{u}_{\rm in} L/\eta$ (blue) over time. The kinematic viscosity ν and resistivity ν are calculated using the formulae given in Table S2 of the Supplementary Information. The input plasma state variables are the experimentally-determined values in the Thomson-scattering volume and $L = 400\,\mu$m; at later times (30 ns, 37.5 ns), $\mathrm{Re_{in}}$ is instead calculated using an extrapolated density derived from the X-ray measurements, and assuming $T_i = T_e$. Errors are calculated in the same way as those for the temperature. Also shown are the results of the FLASH simulations for $\mathrm{Re_{in}}$ and $\mathrm{Rm_{in}}$ (red/blue diamonds).

of the Thomson-scattering probe beam. We were therefore unable to measure $\bar{n}_e$ or Δn_e for times $\gtrsim 30\,$ns using the Thomson-scattering diagnostic. A reasonable estimate of $\bar{n}_e$ can still be obtained, however, using the X-ray framing camera diagnostic. More specifically, assuming that the X-ray emission from the plasma is dominated by bremsstrahlung, we can estimate the mean electron number density $\bar{n}_e(t_1)$ at time t_1 in terms of the mean electron number density $\bar{n}_e(t_2)$ at time t_2 via the following relationship: $\bar{n}_e(t_1) \approx \bar{n}_e(t_2)[\bar{I}(t_1)/\bar{I}(t_2)]^{1/2}$, where $\bar{I}(t)$ is the mean measured intensity on the CCD at time t. Thus, assuming a reference value for $\bar{n}_e(t_2)$ at $t_2 = 29.0\,$ns (derived via linear interpolation from the Thomson-scattering density measurements), we obtain the evolution profile shown in Fig. 5d. The results imply that the density continues to rise for ~ 2 ns after the final Thomson-scattering measurement of density is obtained, reaching a peak value $\bar{n}_e \approx 2.4 \times 10^{20}$ cm^{-3} at $t = 30\,$ns before falling slightly at later times.

We were still able to use the IAW feature to measure the bulk flow velocity and the electron temperature in some spatial locations at later times. The bulk flow velocity was found to drop to $\sim$100 km s^{-1} at 30 ns. At 37.5 ns a similar value was obtained but with a reversed sign; this is possibly due to the Thomson-scattering diagnostic measuring the inflow velocity at a position displaced from the line of centers, which could have an opposite velocity. The electron temperature measured by the Thomson scattering diagnostic remained $\sim$400 eV at later times. However, this is due to heating of the interaction region by the Thomson-scattering beam, which is significant at later times because of the high densities and reduced temperatures. We discuss this effect at greater length in the Supplementary Information with the aid of FLASH simulations.

C. Measuring magnetic fields: proton-imaging diagnostic. The 15.0-MeV proton images for our experiment are presented as a time sequence in the top two rows of Fig. 6. The proton image before the formation of the interaction-region plasma (Fig. 6, 24.2 ns) shows little structure at the center of the grids, which is consistent with the absence of significant magnetic fields. Around the time when the interaction region forms, a moderate diminution of the proton flux is observed in a central region between the grids (Fig. 6, 25.7 ns), with characteristic magnitude Ψ similar to the mean proton flux Ψ_0: $|\Psi - \Psi_0| \lesssim 0.3\Psi_0$. In contrast, in all subsequent proton images (beginning at $t \gtrsim 27.2\,$ns), order-unity variations in the proton flux are measured ($|\Psi - \Psi_0| \gtrsim \Psi_0$) whose structure and position are (at least partially) stochastic – see Fig. 6, 27.2 ns, for an example. This is consistent with a dramatic change in the morphology and strength of the magnetic field.

Further analysis can be performed by reconstructing directly from the measured proton image the (perpendicular) path-integrated field experienced by the imaging proton beam – quantities that are related via a well-known relation (47, 48). Provided the gradients in the magnetic-field strength are not so large as to cause the proton beam to self-intersect before arriving at the detector, this relation leads to an equation of Monge-Ampère type, the unique inversion of which is a well-posed mathematical problem (49) and for which an efficient inversion algorithm exists (48) (we refer to this algorithm as the 'field-reconstruction algorithm'). The results of applying this algorithm to the proton images shown in Fig. 6 are presented in the same figure. The strength and morphology of the reconstructed path-integrated fields after the jet collision are quite different from those at collision, with peak values reaching $\sim$8 kG cm (as opposed to $\sim$1 kG cm at collision) and randomly orientated filamentary structures evident.

With the path-integrated magnetic field having thus been determined, the correct method of estimating the characteristic magnetic-field strength depends on the field structure. The path-integrated field structures evident at early times (i.e., Fig. 7a) are non-stochastic. We therefore follow a standard method for analyzing proton images of non-stochastic mag-

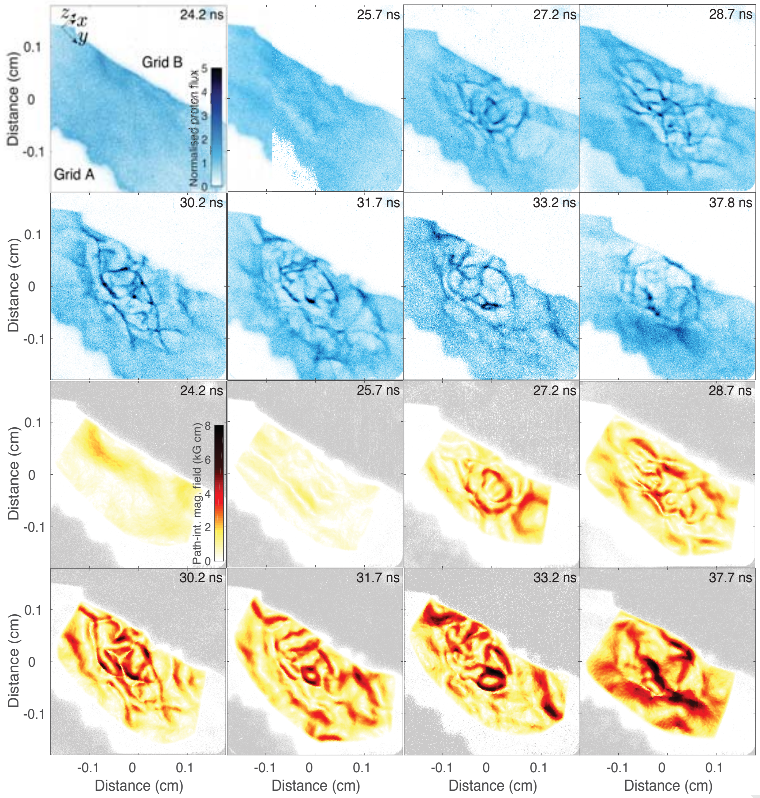

Fig. 6. 15.0 MeV proton images of interaction-region plasma, and extracted path-integrated magnetic fields. The top two rows show the proton images. Each image is approximately 300 $\times$ 300 pixels, with an effective pixel size of $12\,\mu$m; by comparison, the proton-source size is $\sim$40 μm. To prevent confusion, all images are presented with the magnification removed. The grid outline evident on the bottom left of each image is grid A, and the top-right grid is grid B. The mean proton flux Ψ_0 per pixel in these images is ~ 50 protons per pixel The bottom two rows show the magnitude of the path-integrated perpendicular magnetic field, extracted using the field-reconstruction algorithm. The method for applying the field-reconstruction algorithm is as follows. We first select a region of the proton image to analyze; this region is chosen to be as large as possible, within the requirements of staying inside the region of high detected proton flux between the grids, maintaining an approximately rectangular shape, and choosing a boundary that does not intersect regions with high proton flux. We then embed the cropped region of proton flux inside a larger rectangular region, whose size is chosen to be as small as possible while still containing the former region. Values of proton flux are then systematically assigned to pixels outside the cropped region: these values are calculated by linearly interpolating between the nearest actual pixel value and the mean flux of the cropped region of protons. The resulting image is then subjected to a Gaussian high-pass filter, with scale $0.1\,\mathrm{cm}$. This image is then processed with the field-reconstruction algorithm. Subsequent to convergence of the algorithm, the path-integrated field is only retained for pixels inside the original cropped region, with other values removed via a Gaussian window function. These steps are all necessary in order to prevent systemic errors affecting the algorithm (48).

netic fields (50) and consider parameterized models of known three-dimensional magnetic-field structures. To motivate a relevant model for our experimental data, we invoke the expected physical origin of the early-time magnetic fields in the interaction-region plasma: the action of the Biermann battery during the interaction of the drive-beam lasers with the target's foils. This process generates azimuthal magnetic fields in the plane perpendicular to the target's line of centers that are opposite in sign for the two foils (51). These fields are then advected by the two counter-propagating plasma flows towards the midpoint between the two foils. We therefore consider two 'cocoon' structures with magnetic fields of opposite sign, with their symmetry axis parallel to the line of centers.

A simple parameterized model for a double-cocoon configuration considered in (52) takes the form

$$\boldsymbol{B} = \sqrt{2\mathrm{e}}\left[B_{\max}^{+}\mathrm{e}^{-\frac{(z+\ell_c)^2}{b^2}} + B_{\max}^{-}\mathrm{e}^{-\frac{(z-\ell_c)^2}{b^2}}\right]\frac{r}{a}\mathrm{e}^{-\frac{r^2}{a^2}}\boldsymbol{e}_\phi\,, \quad [3]$$

where (r, ϕ, z) is a cylindrical coordinate system with symmetry axis z, $B_{\max}^{+}$ is the maximum magnetic-field strength of the cocoon centered at $z = -\ell_c < 0$, $B_{\max}^{-}$ is the maximum magnetic-field strength of the cocoon centered at $z = \ell_c > 0$, a the characteristic perpendicular size of both cocoons, b their characteristic parallel size, and $\boldsymbol{e}_\phi$ the azimuthal unit vector. It can be shown (see Supplementary Information) that, if $a \gtrsim b$, then the path-integrated magnetic field associated with the double-cocoon configuration, when viewed at the $\theta = 55^\circ$ angle with respect to its symmetry axis, as was done in our experiment (see Materials and Methods), is orientated predominantly perpendicularly to the direction of the line of centers projected onto the proton image, and its strength varies predominantly in the parallel direction (viz., the path-integrated field is quasi 1D). Both of these findings are consistent with the observed structure at the point of maximum path-integrated field (see Fig. 7b), validating our choice of model.

Having obtained a quasi-1D model for the path-integrated magnetic field (which has four free parameters: $B_{\max}^{+}b$, $B_{\max}^{-}b$, a and ℓ_c – see Supplementary Information), we compare it with a lineout across the strongest path-integrated magnetic-field structure (see Fig. 7b). Fig. 7c shows the lineout, as well as the model with an optimized fit: $B_{\max}^{+}b = -0.31 \pm 0.02\,\mathrm{kG}$ cm, $B_{\max}^{-}b = 0.20 \pm 0.02\,\mathrm{kG}$ cm, $a = 270 \pm 19\,\mu\mathrm{m}$, and $\ell_c = 131 \pm 9\,\mu\mathrm{m}$ (here the errors in the model parameters correspond to the 95% confidence intervals). The agreement of the model with these parameters is reasonable, with an adjusted R-squared value of 0.97. Further validation is provided in the Supplementary Information (Fig. S9). The parameterized magnetic-field model itself has an additional free parameter b to be determined; this is done by assuming that the entire magnetic-field configuration is contained inside the interaction-region plasma, and so $b = \ell_n/2 \approx 0.01\,\mathrm{cm}$. The double-cocoon configuration for this choice of b is shown in Fig. 7d. The mean magnetic-field strength associated with the double-cocoon configuration can then be shown to be $\sim$6 kG. This magnetic-field structure and its strength are reproduced successfully by FLASH simulations, although significant small-scale fields are also seen in the simulations that were not detected experimentally (see Fig. S11).

For the stochastic path-integrated magnetic fields that emerge after the jet collision (due to the interaction of the initial seed fields with stochastic fluid motions), a different approach is required: we assume statistically isotropic, homogeneous, tangled magnetic fields in the interaction-region

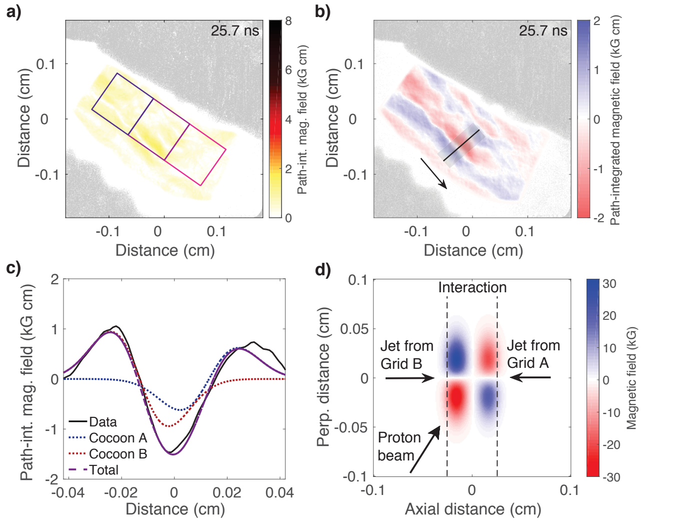

Fig. 7. Path-integrated magnetic fields at the moment of the interaction-region plasma's coalescence. **a)** Magnitude of path-integrated perpendicular magnetic field 25.7 ns after drive-beam pulse initiation. The three square regions in which the average path-integrated field is evaluated have an edge length of 800 μm, and are orientated at 35° to the horizontal axis of the path-integrated field map. The center of the middle square region corresponds to the center of the proton image. **b)** Component of the path-integrated magnetic field in the direction perpendicular to the projected line of centers. This component is calculated from the full 2D perpendicular path-integrated magnetic field. The arrow indicates the (positive) direction of the chosen path-integrated field component. **c)** 1D lineout of the path-integrated field component given in b) (black, solid line) calculated by averaging across its width the semi-transparent rectangular region denoted in a). The path-integrated field associated with model Eq. [3] is also plotted, using optimized parameters $B_{\max}^{+} b = -0.31\,\mathrm{kG\ cm}$, $B_{\max}^{-} b = 0.20\,\mathrm{kG\ cm}$, $a = 270\,\mu\mathrm{m}$, and $l_c = 131\,\mu\mathrm{m}$. The total contribution is plotted (purple, dashed), as well as the individual contributions from the cocoons nearer grid A (blue, dotted), and nearer grid B (red, dotted). **d)** Slice plot (in the plane of basis vectors $\hat{\boldsymbol{y}}$ and $\hat{\boldsymbol{z}}$) of B_x component associated with 3D double-cocoon magnetic-field model given by Eq. [3], with the same model parameters as shown in c), and $b = 0.01\,\mathrm{cm}$. The width of the plotted interaction region is obtained from the X-ray image recorded at the equivalent time (cf. Fig. 2c).

plasma (an assumption verified in Fig. S10), which in turn allows for the unique extraction of the RMS magnetic field strength B_{rms} via the following formula:

$$B_{\mathrm{rms}}^2 = \frac{2}{\pi l_p} \int \mathrm{d}k\, k E_{\mathrm{path}}(k), \qquad [4]$$

where l_p is the path length of the protons through the interaction region, $E_{\mathrm{path}}(k)$ is the 1D spectrum of a given of path-integrated field under normalization condition $\int \mathrm{d}k\, E_{\mathrm{path}}(k) = (\int \mathrm{d}^2\boldsymbol{x}\, \boldsymbol{B}_\perp)^2_{rms}$ (48). We estimate l_p at a given time using our measurements of the average interaction-region width l_n derived from the X-ray imaging diagnostic, combined with the known angle $\theta_p \approx 55^\circ$ of the proton beam through the interaction region with respect to the line of centers (see Materials and Methods): it follows that $l_p \approx l_n/\cos\theta_p \approx 1.7 l_n$. We can then calculate the characteristic correlation length ℓ_B of the stochastic magnetic field via

$$\ell_B = \frac{1}{\ell_p B_{\mathrm{rms}}^2} \int \mathrm{d}k\, E_{\mathrm{path}}(k) \qquad [5]$$

and determine the complete magnetic-energy spectrum $E_B(k)$ from $E_{\mathrm{path}}(k)$ via

$$E_B(k) = \frac{1}{4\pi^2 \ell_p} k E_{\mathrm{path}}(k)\,. \qquad [6]$$

However, we caution that due to the likely presence of strong, small-scale magnetic fields leading to self-intersection of the imaging beam, the power spectrum at wavenumbers $k \gtrsim \pi\ell_B^{-1}$ determined via Eq. [6] is not a faithful representation of the true magnetic-energy spectrum (48). We therefore focus on measuring B_{rms} and ℓ_B. We consider the three fixed regions of the path-integrated magnetic field images introduced in Fig. 7a, and calculate B_{rms} and ℓ_B for those regions.

The mean values of B_{rms} and ℓ_B arising from each path-integrated field image (and the errors on those measurements) for the full time-sequence of path-integrated field images (see Fig. 6) are shown in Fig. 8a. B_{rms} jumps significantly in a 1.5-ns interval subsequent to collision, reaching a peak value $\sim$120 kG, before decaying somewhat, to around $\sim$70 kG. The correlation length has characteristic value $\ell_B \approx 0.01\,\mathrm{cm}$ for all measured times, except at 38 ns. The FLASH simulations, which give similar values for the magnetic-field strength, give

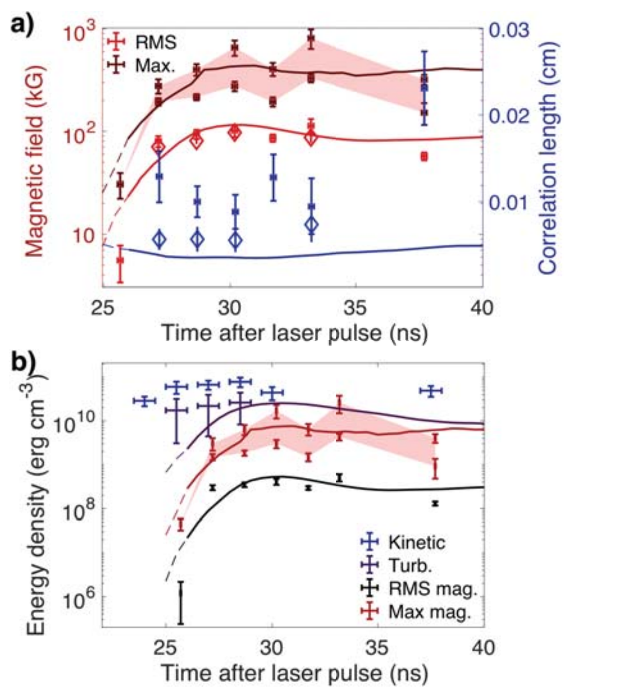

Fig. 8. Magnetic fields subsequent to formation of the interaction-region plasma. a) RMS magnetic-field strength (red data points) and the bounds on the maximum magnetic field (maroon band bounded by maroon data points) versus time, as well as the correlation length ℓ_B (blue data points). We emphasize that the mean and maximum field strengths at 25.7 ns are calculated differently than at the other times, on account of the non-stochastic field structure (see Fig. 7). Also shown are the evolution of the RMS magnetic field (red curve), maximum magnetic field (maroon curve) and correlation length (blue curve) versus time given by FLASH simulations of the experiment. The dashed portions of these curves correspond to times when the plasma in the interaction region is not yet fully collisional and therefore the simulations are not formally valid (see Supplementary Information). In addition, the RMS magnetic field and correlation length determined from simulated proton images of the FLASH simulations are shown as blue/red diamonds (see Fig. S26 of the Supplementary Information). **b)** Evolution of energy densities in the plasma-interaction region versus time. For times $\leq 30\,\mathrm{ns}$, the bulk and turbulent kinetic energy densities are calculated using the values of the plasma state variables derived from the Thomson-scattering diagnostic; at later times, the plasma density required to calculate these energies is determined using the X-ray imaging diagnostic. Also shown are the evolution of the RMS magnetic energy (black curve), maximum magnetic energy (red curve) and turbulent kinetic energy (purple curve) versus time for the FLASH simulations. The dashed portions of these curves have the same meaning as in b). In both a) and b), the experimental values are shown as time intervals with vertical error bars.

a smaller value for the correlation length ($\ell_B \approx 0.004\,\mathrm{cm}$), a discrepancy discussed in Interpretation of Results.

We can also calculate reasonable upper and lower bounds of the maximum magnetic-field strength realized in the stochastic field, via two different methods. For the lower bound, we note that the kurtosis of the path-integrated magnetic field will always be smaller than the kurtosis of the actual magnetic field. Therefore, the ratio between the maximum path-integrated field and the RMS path-integrated field will always be smaller than the equivalent ratio for the magnetic field: in other words, a reasonable lower bound is $B_{\mathrm{max,l}} = B_{\mathrm{rms}}(\int \mathrm{d}^2\boldsymbol{x}\,\boldsymbol{B}_\perp)_{\mathrm{max}}/(\int \mathrm{d}^2\boldsymbol{x}\,\boldsymbol{B}_\perp)_{\mathrm{rms}}$. The upper bound is derived by assuming that the maximum measured path-integrated magnetic field is obtained when the imaging protons cross just a single magnetic structure: $B_{\mathrm{max,u}} = (\int \mathrm{d}^2\boldsymbol{x}\,\boldsymbol{B}_\perp)_{\mathrm{max}}/\ell_B$. These bounds are shown in Fig. 8a. At the time corresponding to maximal B_{rms}, we find $310\,\mathrm{kG} < B_{\mathrm{max}} < 810\,\mathrm{kG}$.

Interpretation of Results

We conclude that our experimental platform does produce a plasma that manifests stochastic motion across a range of scales. In spite of some uncertainty about the late-time physical properties of the turbulent plasma, there exists a 4-ns time interval that starts from the formation of the interaction region and during which the plasma state can be thoroughly characterized by our experimental diagnostics. In this interval, we find that the plasma is fairly well described as classical and collisional ($\lambda_e \approx 10\,\mu\mathrm{m}$, $\lambda_{\mathrm{CC}} \approx 0.6\,\mu\mathrm{m}$, $\lambda_{\mathrm{HC}} \approx 16\,\mu\mathrm{m}$, where λ_e, λ_{CC}, and λ_{HC} are the electron, carbon-carbon and hydrogen-carbon mean free paths respectively), so its transport coefficients can be estimated (see Supplementary Information) using collisional transport theory (53–55). Momentum transport in the plasma is dominated by hydrogen ions, on account of their long mean free path compared to carbon ions (56, 57), while heat transport is dominated by electrons.

The time history of the fluid Reynolds number $\mathrm{Re_{in}} = \bar{u}_{\mathrm{in}}L/\nu$ and the magnetic Reynolds number $\mathrm{Rm_{in}} = \bar{u}_{\mathrm{in}}L/\eta$ in our experiment (which are defined here using the inflow velocity $\bar{u}_{\mathrm{in}}$ in order to enable comparisons between the state of the plasma both before and after the two plasma flows collide to form the interaction-region plasma) is shown in Fig. 5f. Prior to the collision of the plasma flows, $\mathrm{Re_{in}} = (1.2 \pm 0.6) \times 10^3$, which exceeds $\mathrm{Rm_{in}} = 210 \pm 60$. However, after the formation of the interaction-region plasma, the rapid collisional shock heating of both ions and electrons simultaneously decreases the resistivity and enhances the viscosity, leading to the opposite ordering of dimensionless numbers: $\mathrm{Re_{in}} = 280 \pm 180$ and $\mathrm{Rm_{in}} = 890 \pm 220$, so $\mathrm{Pm} = \mathrm{Rm_{in}}/\mathrm{Re_{in}} = 3.1 \pm 2.0$. The characteristic velocity u_{rms} of stochastic motions is smaller than the in-flow velocity, and thus the fluid Reynolds number $\mathrm{Re} = u_{\mathrm{rms}}L/\nu$ and magnetic Reynolds number $\mathrm{Rm} = u_{\mathrm{rms}}L/\eta$ of the driving-scale stochastic motions are somewhat smaller than $\mathrm{Re_{in}}$ and $\mathrm{Rm_{in}}$: $\mathrm{Re} = 150 \pm 110$ and $\mathrm{Rm} \approx 450 \pm 220$. We observe that at such Re, turbulence is not ‘fully developed’ in the asymptotic sense. However, this is not necessary for the fluctuation dynamo to operate: the fluid motions need only be stochastic (19). Pm remains order unity for $t \lesssim 30\,\mathrm{ns}$; since the turnover time τ_L of the largest stochastic motions is $\tau_L = L/u_{\mathrm{rms}} \approx 4\,\mathrm{ns}$, we conclude that the experimental platform does indeed produce a region of plasma with $\mathrm{Pm} \gtrsim 1$, which survives longer than the timescale on which the largest-scale stochastic motions decorrelate.

We have measured the magnetic field’s evolution with time in the interaction-region plasma, and found that field strengths are amplified tenfold from their initial values during the 4-ns time window after collision. Having measured both the magnetic field and dynamical properties of the interaction-region plasma, we can compare the time history of the turbulent and magnetic energy densities (see Fig. 8b). When the interaction-region plasma initially coalesces, the turbulent kinetic energy density $\varepsilon_{\mathrm{turb}} \equiv \rho u_{\mathrm{rms}}^2/2 = (1.7 \pm 1.4) \times 10^{10}\,\mathrm{erg/cm^3}$ is many orders of magnitude larger than the average magnetic-energy density associated with seed Biermann fields [$\varepsilon_B = B^2/8\pi = (1.2 \pm 1.0) \times 10^6\,\mathrm{erg/cm^3}$], implying that the latter is not dynamically significant. However, 1.5 ns later, the relative magnitude of the magnetic energy is significantly larger: $\varepsilon_B/\varepsilon_{\mathrm{turb}} = 0.015 \pm 0.012$. Furthermore, the FLASH simulations of our experiment – which successfully reproduce the evolution of hydrodynamic variables and exhibit dynamo action that results in similar energy ratios – indicate that the magnetic field at the end of the 4-ns time window is dynamically significant in at least some locations in the plasma (see Fig. S21). We therefore claim to have demonstrated the operation of a fluctuation dynamo in a $\mathrm{Pm} \gtrsim 1$ plasma.

We can use the experimental data to infer the exponential growth rate γ that would be consistent with the observed evolution of the magnetic-field strength. Noting its value both at collision ($B_{t=25.7\,\mathrm{ns}} \approx 6\,\mathrm{kG}$) and 1.5 ns later ($B_{t=27.2\,\mathrm{ns}} \approx 86\,\mathrm{kG}$), we find $\gamma \gtrsim 6.7 \log\left(B_{t=27.2\,\mathrm{ns}}/B_{t=25.7\,\mathrm{ns}}\right) \times 10^8\,\mathrm{s^{-1}} = (1.8 \pm 0.4) \times 10^9\,\mathrm{s^{-1}} \approx 4\text{–}12 u_{\mathrm{rms}}/L$. This growth is more efficient than that predicted by periodic-box MHD simulations of the $\mathrm{Pm} \approx 1$ fluctuation dynamo with similar parameters, in which $\gamma \approx 0.3\text{–}2 u_{\mathrm{rms}}/L$ (20, 21, 24, 25). We attribute this discrepancy to strong shear flows in the interaction-region plasma, directed parallel to the line of centers, in addition to stochastic motions. While a 2D uni-directional shear flow cannot account for sustained amplification of magnetic fields, its coupling to other stochastic plasma motions (including KH-unstable modes associated with the shear flow) can enable dynamo action. On account of our approach for diagnosing turbulence via side-on X-ray imaging of the interaction-region plasma, we do not have a direct experimental measurement of these shear flows; such a measurement might be possible in future experiments utilizing alternative diagnostic approaches. However, the FLASH simulations – which show exponential growth of the field at a similar rate to that inferred from the experimental data – support this interpretation (see Supplementary Information): the RMS rate of strain of the simulated velocity field, which follows the growth rate of the magnetic energy, is comparable to the rate of strain of the directed shear flows. Shear flows are common in astrophysical plasmas, so enhanced magnetic-field amplification on account of their interaction with turbulence may be relevant to astrophysical systems such as galaxy clusters (58).

Another noteworthy finding of our experiments is the characteristic scale of the amplified stochastic magnetic fields, which is a factor of $\sim$2–3 times larger than is measured in periodic-box MHD simulations. The integral scale $L_{\mathrm{int,B}} \equiv 4\ell_B$ of the magnetic fields that we measure is the same as the driving scale L of the stochastic motions: $L_{\mathrm{int,B}} = 400 \pm 80\,\mu\mathrm{m} \approx 0.6\text{–}1.4L$; the comparable value in the saturated state of periodic-box MHD simulations is robustly found to be $L_{\rm int,B} \approx 0.3L$ at similar Rm and Pm (22, 25). The characteristic value of the integral scale obtained directly from the FLASH simulations of our experiment, in which the magnetic-energy spectrum evolves similarly in time to the previous periodic-box simulations (see Supplementary Information, Fig. S22), is also smaller than the experimentally measured value. Part of this apparent discrepancy is an artifact of technical issues that can inhibit accurate determination of the high-wavenumber tail of the magnetic-energy spectrum from proton-imaging data (see Fig. S23). Extracting path-integrated field maps from simulated proton images of the FLASH simulations and subsequently inferring the correlation length using the same approach applied to the experimental data, we find closer agreement (see Fig. 8a, blue diamonds), which suggests a possible overestimation of the correlation lengths attained experimentally. Yet some discrepancy in the inferred correlation length remains, particularly at early times. The robustness of this discrepancy is confirmed by direct analysis of simulated proton images of the FLASH simulations (Fig. S24), or the magnetic-energy spectra inferred from both experimental and simulated path-integrated field maps (Fig. S25). This result is tantalizing, given the long-standing problem of explaining the observed scale of tangled magnetic fields present in the ICM (59): current ICM simulations tend to predict magnetic fields at smaller scales than observed (60, 61).

A simple possible explanation for why the characteristic scale of the magnetic fields in the FLASH simulations is smaller at early times than in our experiment arises from the presence of small-scale seed magnetic fields in the latter just after the jet collision that are not observed experimentally (see Section C). We attribute this difference to the fact that the results of a one-fluid MHD code such as FLASH are not a valid model of the interaction region before collisional thermalization between the two jets has occurred (which, as we show in the Supplementary Information, takes place by $t \approx 26.5$ ns). Recent work (62) shows that the magnetic-energy spectrum and the correlation length associated with the dynamo-amplified fields are time-dependent functions of the initial spectrum of seed fields for the degree of magnetic-energy amplification we realize in our experiment. Thus the small-scale seed fields present in the FLASH simulations but not in the experimental data could cause the correlation length in the FLASH simulations to be smaller than in the experiment for a period post collision. Other possible explanations include additional physical processes that could arise due to the order-unity Hall parameter being attained subsequent to the seed field's amplification (63), or differences in the mechanism of resistive dissipation between the experiments and the simulations enabling a more efficient inverse magnetic-energy cascade in the former (64).

Finally, we note that the maximum measured ratio of ε_B to $\varepsilon_{\rm turb}$ – at $t \approx 28.7$ ns, which is also the latest time at which such a measurement was successfully made in the experiment – is $\varepsilon_B/\varepsilon_{\rm turb} = 0.03 \pm 0.02$. This value, which is also obtained (but not surpassed, even at later times) in the FLASH simulations, is a factor of a few smaller than that obtained for Pm ≈ 1 MHD simulation at saturation with comparable Reynolds numbers ($\varepsilon_B/\varepsilon_{\rm turb} \approx 0.08$) (25). There are two possible explanations for the lower measured values of $\varepsilon_B/\varepsilon_{\rm turb}$ in the experiment. First, the time at which this measurement is taken is less than a single driving-scale eddy turnover time after the turbulent plasma is formed; thus, it is likely that insufficient time has passed for the saturated state of the fluctuation dynamo to be obtained in the experiment. Second, due to conductive losses, the plasma cools significantly for times $\gtrsim 30$ ns, attaining characteristic temperatures $T_e \approx T_i \approx 80\,\mathrm{eV}$ at $t = 37.5$ ns (in the absence of heating by the Thomson-scattering probe beam – see Supplementary Information). Since both Rm $\propto T_e^{3/2}$ and Pm $\propto T_e^{3/2} T_i^{5/2}$ are sensitive functions of temperature, this cooling results in a transition to a different parameter regime: Rm ≈ 20, and Pm $\approx 10^{-3}$. This transition should inhibit dynamo action, although to our knowledge, such a transition occurring during the nonlinear phase of the fluctuation dynamo has not been studied previously.

In summary, our experiment supports the notion that turbulent plasma with Pm $\gtrsim 1$ and sufficiently large Rm is capable of amplifying magnetic fields up to dynamical strengths. Furthermore, the time-resolved characterization provided by the experiment has demonstrated that magnetic-field amplification in the plasma occurs at a much larger rate than the stretching rate associated with the outer scale of the turbulent motions. This rate of growth is greater than is typically obtained in periodic-box MHD simulations with equivalent Mach number, Rm, and Pm, a finding that we attribute to the presence of strong directed shears in the interaction-region plasma. The characteristic scale of these fields is found to be larger than anticipated by resistive-MHD simulations, including our MHD FLASH simulations of the experiment, which otherwise faithfully reproduce the plasma's evolution. Both findings suggest that the fluctuation dynamo – when operating in realistic plasma – may be capable of generating large-scale magnetic fields more efficiency than currently expected by analytic theory or MHD simulations.

Materials and Methods

X-ray framing camera specifications. Images of self-emitted soft X-rays from the interaction-region plasma were recorded using a framing camera (65, 66) configured with a two-strip microchannel plate (MCP) (67) and a 50 μm pinhole array. The pinhole array was situated 9.14 cm away from the center of the target and the main detector at 27.4 cm, giving rise to a $\times 2$ image magnification. A thin filter composed of 0.5 μm polypropene and 150 nm of aluminum was placed in front of the MCP, removing radiation with photon energy $\lesssim 100\,\mathrm{eV}$. The MCP itself was operated with a 1 ns pulse-forming module at a constant 400 V bias, and the two strips sequentially gated: this allowed for two images (time-integrated over a 1 ns interval) of the plasma at pre-specified times to be detected for each experimental shot. Electrons exiting the MCP struck a phosphor plate, producing an optical image, which was recorded using a 4096 $\times$ 4096 9-μm pixel charge-coupled-device (CCD) camera. The chosen voltage bias was such that the response of the CCD camera was linear and thus the relative counts of two given pixels provided a measure of the relative (optical) intensity incident on the CCD. To allow comparison between the X-ray images of the interaction-region plasma at different stages of its evolution, the framing-camera bias was fixed throughout the experiment and its value optimized for probing the interaction-region plasma at peak emission. Given this normalization and the measured signal-to-noise ratio, the effective dynamic range of the camera was $\sim$100. The frequency-response curves of various components of the X-ray framing camera, along with the combined response, are shown in Fig. S1a of the Supplementary Information.

Thomson-scattering diagnostic specifications. The Thomson-scattering diagnostic employed a 30 J, frequency-doubled (526.5 nm) laser, which probed the plasma in a cylindrical volume with cross-sectional area 50 μm^2 and length 1.5 mm centered on the target's center, which coincided with the target-chamber centre (TCC). The orientation of the scattering volume is shown in Fig. 1. The scattered light was collected at scattering angle 63°. As mentioned in Experimental Design, the Thomson-scattering signal was resolved spatially along the cylindrical scattering volume and integrated over the 1 ns duration of the laser pulse. The high- and low-frequency components of the spectrum were recorded separately using two distinct spectrometers; the separation was performed using a beam splitter.

Thomson-scattering data analysis. To interpret the IAW and EPW features, a theory relating the scattered laser light detected at a particular wavelength – or, equivalently, frequency – to fundamental properties of the plasma is needed. For a given scattering vector $\boldsymbol{k}$, it can be shown (68) that the spectrum $I(\boldsymbol{k},\omega)$ of the laser light scattered by the plasma at frequency ω is given by

$$I(\boldsymbol{k},\omega) = N_e I_0 \sigma_{\mathrm{T}} S(\boldsymbol{k},\omega)\,, \qquad [7]$$

where N is the total number of scattering electrons, I_0 the intensity of the incident laser, $\sigma_T \equiv (q_e^2/m_e c)^2 \sin^2\vartheta_{\mathrm{T}}$ the Thomson cross-section for scattering by a free electron (q_e is the elementary charge, m_e the electron mass, c the speed of light, and ϑ_{T} the angle between the direction of the electric field of the incident and scattered light), and

$$S(\boldsymbol{k},\omega) \equiv \frac{1}{2\pi N_e}\int \mathrm{d}t\, \exp\left[\mathrm{i}(\omega-\omega_0)t\right]\langle n_e(\boldsymbol{k},0) n_e(\boldsymbol{k},t)^*\rangle \qquad [8]$$

is the dynamic form factor (ω_0 being the frequency of the incident light). Assuming that the distribution functions of the electrons and ions are close to shifted Maxwellian distributions, with electron number density n_e, electron temperature T_e, temperature T_j of ion species j, and bulk fluid velocity $\boldsymbol{u}$, and also that the Debye length is $\lambda_{\mathrm{D}} \lesssim 10^{-6}$ cm (assumptions justified by Table S2 of the Supplementary Information), we find that $\alpha \equiv 1/k\lambda_{\mathrm{D}} \gtrsim 8 > 1$; thus, we can employ the Salpeter approximation for the dynamic form factor (68):

$$\begin{aligned} S(\boldsymbol{k},\omega) \quad \approx \quad & \frac{1}{kv_{\mathrm{the}}}\Gamma_{\alpha}\left(\frac{\tilde{\omega}-\omega_0}{kv_{\mathrm{the}}}\right) \\ & + \sum_j \frac{Z_j}{kv_{\mathrm{th}j}}\left(\frac{\alpha^2}{1+\alpha^2}\right)^2 \Gamma_{\bar{\alpha}_j}\left(\frac{\tilde{\omega}-\omega_0}{kv_{\mathrm{th}j}}\right), \qquad [9] \end{aligned}$$

where $\tilde{\omega} \equiv \omega - \boldsymbol{k}\cdot\boldsymbol{u}$ is the Doppler-shifted frequency, the sum is over all ion species in the plasma, Z_j is the charge of ion species j,

$$\Gamma_{\alpha}(x) \equiv \frac{\exp\left(-x^2\right)}{\sqrt{\pi}\left|1+\alpha^2[1+xZ(x)]\right|^2}\,, \qquad [10]$$

and $\bar{\alpha}_j = Z_j\alpha^2 T_e/T_j(1+\alpha^2)$. The complex function $Z(x)$ is the plasma dispersion function (69). For low-frequency fluctuations (in particular, ion-acoustic waves), $\omega-\omega_0 \sim kv_{\mathrm{th}j}$ and so the first term on the right-hand side of [9] is small by a factor of $\mathcal{O}[Z_i(m_eT_i)^{1/2}/(m_iT_e)^{1/2}] \ll 1$ when compared to the second (this factor is indeed small provided the ion temperature T_i – assumed equal for all ion species – is comparable to the electron temperature); thus the shape of the low-frequency spectrum is dominated by the second term. For high-frequency fluctuations (electron plasma waves) satisfying $\omega-\omega_0 \sim kv_{\mathrm{the}}$, the second term is smaller than the first by an exponential factor $\mathcal{O}[\exp(-m_eT_i/m_iT_e)] \ll 1$; thus the shape of the high-frequency spectrum is dominated by the first term. We conclude that we can relate physical properties of the plasma to the measured EPW and IAW features using fits given by the first and second terms of [9], respectively.

However, for our experiment, there is a complication: the presence of stochastic motions and density fluctuations. The presence of such fluctuations means that the bulk fluid velocity $\boldsymbol{u}$ and electron density n_e are not necessarily fixed parameters inside the Thomson-scattering volume during the time-integrated measurement, but instead possess a range of values. To account for this range, we assume that fluctuations of velocity and density are isotropic and normally distributed, with means $\bar{\boldsymbol{u}}$ and $\bar{n}_e$, and standard deviations Δu and Δn_e, respectively. Under this assumption, the appropriate fit for the IAW feature is

$$\begin{aligned} S_{\mathrm{IAW}}(\boldsymbol{k},\omega) \quad \approx \quad & \frac{\sqrt{3}}{\sqrt{\pi}\Delta u}\int \mathrm{d}\tilde{U}_{\parallel}\, \exp\left[-\frac{3(\tilde{U}_{\parallel}-\bar{u}_{\parallel})^2}{\Delta u^2}\right] \\ \times \quad & \sum_j \frac{Z_j}{kv_{\mathrm{th}j}}\frac{\alpha^4}{(1+\alpha^2)^2}\Gamma_{\bar{\alpha}_j}\left(\frac{\omega - k\tilde{U}_{\parallel}-\omega_0}{kv_{\mathrm{th}j}}\right), [11] \end{aligned}$$

where $\bar{u}_{\parallel} \equiv \hat{\boldsymbol{k}}\cdot\boldsymbol{u}$. For the EPW feature, we use

$$\begin{aligned} S_{\mathrm{EPW}}(\boldsymbol{k},\omega) \quad \approx \quad & \frac{1}{\sqrt{\pi}\Delta n_e}\int \mathrm{d}\tilde{n}_e\, \exp\left[-\frac{(\tilde{n}_e-\bar{n}_e)^2}{\Delta n_e^2}\right] \\ & \times \frac{1}{kv_{\mathrm{the}}}\Gamma_{\alpha}\left(\frac{\omega-\omega_0}{kv_{\mathrm{the}}}\right). \qquad [12] \end{aligned}$$

In spite of the seeming complexity of these equations, for a fully ionized CH plasma the spectral shapes implied by [11] and [12] are quite simple: a double peak structure, where the position and width of the peaks depend on plasma parameters. For the IAW feature, the distance between the peaks provides a measure of T_e; the shift in the position of the double-peaked spectrum with respect to the incident probe beam's frequency gives a measurement of the bulk velocity $\bar{u}_{\parallel}$; the width of both peaks is a function of both T_i and of the small-scale stochastic velocity dispersion Δu. The effect of the density on the shape of the IAW feature is negligible. For the EPW feature, the opposite holds: the position of the peak is determined by n_e. The width of the peak is in general determined by a range of factors – Landau damping, collisions and the range of fluctuating densities Δn_e. For our experiment, both collisional broadening and that by Landau damping are small (because $k\lambda_e \gg 1$ and $\alpha^2 \gg 1$, respectively), but the spread of densities can be significant. The fitting procedure is described in the Supplementary Information.

Proton-imaging diagnostic specifications. The proton imaging diagnostic was implemented by imploding a D^3He capsule (70): the capsule (diameter 420 μm) is composed of 2 μm of SiO_2 (coated with aluminum), and filled with 18 atm D^3He gas (6 atm D_2 and 12 atm ^3He). The capsule is imploded using 17, 270 J beams, each with a 600 ps pulse length, and 1.82 mm defocus. This results in the generation of $\sim 10^9$ 3.3 MeV and 15.0 MeV protons via nuclear fusion reactions. These protons rapidly travel outward from the center of the backlighter as a uniform spherical sheet, passing through the plasma-filled volume, before reaching a detector composed of interleaved metal sheets and solid-state nuclear track detector, CR-39 (71) (chemical formula $C_{12}H_{18}O_7$). The specific design of the detector is as follows: 7.5 μm of tantalum, then 1.5 mm of CR-39, then 150 μm of aluminum, and finally another 1.5 mm of CR-39. This design ensures that 3.3 MeV protons are stopped in the first layer of CR-39, and 15.0 MeV protons in the second; the tantalum filter minimizes damage to the CR-39 resulting from X-rays. Highly charged ions deposit the majority of their energy close to where they are stopped completely, leaving small tracks of broken molecular bonds. The positions of these tracks is determined by etching the CR-39 for two to three hours in a 6N solution of sodium hydroxide, yielding tracks with diameters $\sim 10\,\mu$m. An automated microscope system records the location of tracks, before removing image defects and counting the number of protons in preset bin sizes: the output are proton (fluence) images. The robust design of the detector is such that protons reaching the detector are recorded with close to 100% efficiency. The dimensions of the imaging set-up are as follows: the distance r_i from the proton source to the center of the target is $r_i = 1$ cm, and the distance from the proton source to the detector is 28 cm. The magnification of the imaging set-up is thus $\times 28$. The geometry of the target is such that the line connecting the center of the proton source to the target's geometric center is at an angle $\theta_p = 55°$ to the z axis. On account of the comparatively large distance of the proton source from the target's center ($r_i = 1$ cm) compared to the transverse extent of the interaction-region plasma ($l_{n\perp} \lesssim 0.3$ cm), which is centered on the target's geometric center, the deviation of the angle of any imaging proton passing through the interaction region with respect to θ_p is $\lesssim 6°$.

ACKNOWLEDGMENTS. The research leading to these results has received funding from the European Research Council under the

European Community's Seventh Framework Programme (FP7/2007-2013)/ERC grant agreements no. 256973 and 247039, the U.S. Department of Energy (DOE) National Nuclear Security Administration (NNSA) under Contract No. B591485 to Lawrence Livermore National Laboratory (LLNL), Field Work Proposal No. 57789 to Argonne National Laboratory (ANL), Subcontract No. 536203 with Los Alamos National Laboratory, Subcontract B632670 with LLNL, and grants No. DE-NA0002724, DE-NA0003605, and DE-NA0003934 to the University of Chicago, DE-NA0003868 to the Massachusetts Institute of Technology, and Cooperative Agreement DE-NA0003856 to the Laboratory for Laser Energetics University of Rochester. We acknowledge support from the U.S. DOE Office of Science Fusion Energy Sciences under grant No. DE-SC0016566 and the National Science Foundation under grants No. PHY-1619573, PHY-2033925, and AST-1908551. Awards of computer time were provided by the U.S. DOE ASCR Leadership Computing Challenge (ALCC) program, using resources at ANL, which is supported by the U.S. DOE Office of Science under contract No. DE-AC02-06CH11357. We acknowledge funding from grants 2016R1A5A1013277 and 2017R1A2A1A05071429 of the National Research Foundation of Korea. Support from AWE plc., the Engineering and Physical Sciences Research Council (grant numbers EP/M022331/1, EP/N014472/1, and EP/R034737/1) and the U.K. Science and Technology Facilities Council is also acknowledged.

1. R Beck, Magnetic fields in spiral galaxies, *Astron. Astrophys. Rev.* **24**, 1 (2015)
2. V Vacca *et. al.* Magnetic fields in galaxy clusters and in the large-scale structure of the universe, *Galaxies* **6**, 142 (2018)
3. L Biermann, and A Schluter, Cosmic radiation and cosmic magnetic fields. II. Origin of cosmic magnetic fields, *Phys. Rev.* **29**, 29 (1951)
4. RM Kulsrud, R Cen, JP Ostriker and D Ryu, The protogalactic origin for cosmic magnetic fields, *Astrophys. J.* **480**, 481 (1997)
5. R Kulsrud, A critical review of galactic dynamos, *Annu. Rev. Astron. Astrophys.* **37**, 37 (1999)
6. K Subramanian, From primordial seed magnetic fields to the galactic dynamo, *Galaxies* **7**, 47 (2019)
7. K Subramanian, A Shukurov, and NEL Haugen, Evolving turbulence and magnetic fields in galaxy clusters, *Mon. Not. R. Astron. Soc.* **366**, 1437 (2006)
8. D Ryu, H Kang, J Cho, and S Das, Turbulence and magnetic fields in the large-scale structure of the universe, *Science* **320**, 909 (2008)
9. GK Batchelor, On the spontaneous magnetic field in a conducting liquid in turbulent motion, *Proc. R. Soc. A.* **201**, 405 (1950)
10. F Rincon, Dynamo theories, *J. Plasma Phys.* **85**, 205850401 (2019)
11. AP Kazentsev, Enhancement of a magnetic field by a conducting fluid, *Soviet-JETP* **26**, 1031 (1968)
12. SI Vainstein, and YB Zel'dovich, Review of topical problems: origin of magnetic fields in astrophysics (turbulent 'dynamo' mechanisms), *Sov. Phys. Usp.* **15**, 159 (1972)
13. YB Zel'dovich, AA Ruzmaikin, SA Molchanov, and DD Sololov, Kinematic dynamo problem in a linear velocity field, *J. Fluid Mech.* **144**, 1 (1984)
14. R Kulsrud, and SW Anderson, The spectrum of random magnetic fields in the mean field dynamo theory of the galactic magnetic field, *Astrophys. J.* **396**, 606 (1992)
15. M Meneguzzi, U Frisch, and A Pouquet, Helical and nonhelical turbulent dynamos, *Phys. Rev. Lett.* **47**, 1060 (1981)
16. S Kida, S Yanase, and J Mizushima, Statistical properties of MHD turbulence and turbulent dynamo, *Phys. Fluids A* **3**, 457 (1991)
17. RS Miller, F Mashayek, V Adumitroaie, and P Givi, Structure of homogeneous nonhelical magnetohydrodynamic turbulence, *Phys. Plasmas* **3**, 3304 (1996)
18. J Cho, and ET Vishniac, The generation of magnetic fields through driven turbulence, *Astrophys. J.* **538**, 217 (2001)
19. AA Schekochihin, SC Cowley, SF Taylor, JL Maron, and JC McWilliams, Simulations of the small-scale turbulent dynamo, *Astrophys. J.* **612**, 276 (2004)
20. NE Haugen, A Brandenburg, and W Dobler, Simulations of nonhelical hydromagnetic turbulence, *Phys. Rev. E* **70**, 016308 (2004)
21. AA Schekochihin, AB Iskakov, SC Cowley, JC McWilliams, MRE Proctor and TA Yousef, Fluctuation dynamo and turbulent induction at low magnetic Prandtl numbers. *New J. Phys.* **9**, 300 (2007)
22. J Cho, and D Ryu, Characteristic lengths of magnetic field in magnetohydrodynamic turbulence, *Astrophys. J.* **705**, L90 (2009)
23. A Beresnyak, Universal nonlinear small-scale dynamo, *Phys. Rev. Lett.* **108**, 035002 (2012)
24. DH Porter, TW Jones, and D Ryu Vorticity, shocks, and magnetic fields in subsonic, ICM-like turbulence gas motions in the intra-cluster medium, *Astrophys. J.* **810**, 93 (2015)
25. A Seta, PJ Bushby, A Shukurov and TS Wood, On the saturation mechanism of the fluctuation dynamo at Pm > 1, *Phys. Rev. Fluids* **5**, 043702 (2020)
26. AA Ruzmaikin, and DD Sokolov, The magnetic field in mirror-invariant turbulence, *Sov. Astron. Lett.* **7**, 388 (1981)
27. S Boldyrev, and F Cattaneo, Magnetic-field generation in Kolmogorov turbulence, *Phys. Rev. Lett.* **92**, 144501 (2004)
28. AB Iskakov, AA Schekochihin, SC Cowley, JC McWilliams, and MRE Proctor Numerical demonstration of fluctuation dynamo at low magnetic Prandtl numbers, *Phys. Rev. Lett.* **98**, 208501 (2007)
29. C Federrath, J Schober, S Bovino, and DRG Schleicher, The turbulent dynamo in highly compressible supersonic plasmas *Astrophys. J. Lett.* **797**, L19 (2014)
30. J Cho, ET Vishniac, A Beresnyak, A Lazarian, and D Ryu, Growth of magnetic fields induced by turbulent motions, *Astrophys. J.* **693**, 1449 (2009)
31. NE Haugen, A Brandenburg, and W Dobler, Is nonhelical hydromagnetic turbulence peaked at small scales?, *Astrophys. J.* **597**, L141 (2003)
32. G Gregori *et. al.*, Generation of scaled protogalactic seed magnetic fields in laser-produced shock waves, *Nature* **481**, 480 (2012)
33. J Meinecke *et. al.*, Turbulent amplification of magnetic fields in laboratory laser-produced shock waves, *Nat. Phys.* **10**, 520 (2014)
34. J Meinecke *et. al.*, Developed turbulence and nonlinear amplification of magnetic fields in laboratory and astrophysical plasmas, *Proc. Nat. Acad. Sci.* **112**, 8211 (2015)
35. G Gregori, B Reville, and F Miniati The generation and amplification of intergalactic magnetic fields in analogue laboratory experiments with high power lasers, *Phys. Reports.* **601**, 1 (2015)
36. P Tzeferacos *et. al.*, Numerical modeling of laser-driven experiments aiming to demonstrate magnetic field amplification via turbulent dynamo *Phys. Plasmas* **24**, 041404 (2017)
37. P Tzeferacos *et. al.*, Laboratory evidence of dynamo amplification of magnetic fields in a turbulent plasma *Nat. Commun.* **9**, 591 (2018)
38. T Boehly *et. al.*, Initial performance results of the OMEGA laser system, *Optics Communications* **133**, 495 (1997)
39. B Fryxell *et. al.*, FLASH: An Adaptive Mesh Hydrodynamics Code for Modeling Astrophysical Thermonuclear Flashes, *Astrophys. J.* **131**, S273 (2000)
40. P Tzeferacos *et. al.*, FLASH MHD simulations of experiments that study shock generated magnetic fields., *High Energy Dens. Phys.* **17**, 24 (2015)
41. S Müller *et. al.*, Evolution of the design and fabrication of astrophysics targets for turbulent dynamo (TDYNO) experiments on OMEGA *Fusion Sci. Tech.* **73**, 434 (2017)
42. A Rigby, J Katz, AFA Bott, TG White, P Tzeferacos, DQ Lamb, DH Froula, G Gregori. Implementation of a Faraday rotation diagnostic at the OMEGA laser facility, High Power Laser Science and Engineering **6** (2018)
43. GB Rybicki and AP Lightman, Radiative processes in astrophysics. (Wiley-VCH, Weinheim, 2004)
44. E Churazov *et. al.*, X-ray surface brightness and gas density fluctuations in the Coma cluster, *Mon. Not. R. Astron. Soc.* **421**, 1123 (2012)
45. I Zhuravleva *et. al.*, The relation Between gas density and velocity power spectra in galaxy clusters: qualitative treatment and cosmological simulations, *Astrophys. J.* **788**, L13 (2014)
46. TG White *et. al.*, Supersonic plasma turbulence in the laboratory, *Nature Comm.* **10**, 1758 (2019)
47. NL Kugland *et. al.*, Relation between electric and magnetic field structures and their proton-beam images, *Rev. Sci. Instrum.* **83**, 101301 (2012)
48. AFA Bott, C Graziani, TG White, P Tzeferacos, DQ Lamb, G Gregori, and AA Schekochihin Proton imaging of stochastic magnetic fields, *J. Plasma Phys.* **83**, 6 (2017)
49. W Gangbo, and RJ McCann The geometry of optimal transportation, *Acta Math.* **177**, 113-161 (1996)
50. G Sarri *et. al.*, Dynamics of self-generated, large amplitude magnetic fields following high-intensity laser matter interaction, *Phys. Rev. Lett.* **109**, 205002. (2012)
51. JA Stamper *et. al.*, Spontaneous magnetic Fields in laser-produced plasmas, *Phys. Rev. Lett.* **26**, 1012 (1971)
52. NL Kugland *et. al.*, Visualizing electromagnetic fields in laser-produced counter-streaming plasma experiments for collisionless shock laboratory astrophysics, *Phys. Plasmas* **20**, 056313 (2013)
53. SI Braginskii, Transport processes in a plasma, in: M.A. Leontovich (Ed.), Reviews of Plasma Physics, vol. 1. (1965), p. 205.
54. JD Huba, NRL plasma formulary. (Naval Research Laboratory, Washington DC, 1994)
55. DD Ryutov, RP Drake, and J Kane, Similarity criteria for the laboratory simulation of supernova hydrodynamics, *Astrophys. J.* **518**, 821 (1999)
56. AN Simakov and K Molvig, Electron transport in a collisional plasma with multiple ion species. *Phys. Plasmas* **21**, 024503 (2014)
57. AN Simakov and K Molvig, Hydrodynamic description of an unmagnetized plasma with multiple ion species. II. Two and three ion species plasmas. *Phys. Plasmas* **23**, 032116 (2016)
58. A Simionescu *et. al.*, Constraining gas motions in the intra-cluster medium. *Space Sci. Rev.* **215**, 24 (2019)
59. AA Schekochihin, and SC Cowley Turbulence, magnetic fields, and plasma physics in clusters of galaxies, *Phys. Plas.* **13**, 056501 (2006)
60. S Roh, D Ryu, H Kang, S Ha1, and H Jang, Turbulence dynamo in the stratified medium of galaxy clusters *Astrophys. J.* **883**, 138 (2019)
61. F Vazza, G Brunetti, M Bruggen, and A Bonafede, Resolved magnetic dynamo action in the simulated intracluster medium *Mon. Not. R. Astron. Soc.* **472**, 1672 (2018)
62. A Seta, and C Federrath, Seed magnetic fields in turbulent small-scale dynamos, *Mon. Not. R. Astron. Soc.* **499**, 2076 (2020)
63. MG Haines, Magnetic-field generation in laser fusion and hot-electron transport *Can. J. Phys.* **64**, 86 (1986)
64. AA Schekochihin, MHD turbulence: a biased review. arXiv:2010.00699 (01 October 2020)
65. JD Kilkenny, P Bell, R Hanks, G Power, RE Turner, and J Wiedwald, High-speed gated x-ray imagers. *Rev. Sci. Instrum.* **59**, 1793 (1988)
66. DK Bradley, PM Bell, OL Landen, JD Kilkenny and J Oertel, Development and characterization of a pair of 30–40 ps x-ray framing cameras. *Rev. Sci. Instrum.* **66**, 716 (1995)
67. GA Rochau *et. al.*, Energy dependent sensitivity of microchannel plate detectors. *Rev. Sci. Instrum.* **802**, 323 (2006)
68. DE Evans and J Katzenstein, Laser light scattering in laboratory plasmas. *Rep. Prog. Phys.* **32**, 207 (1969).
69. BD Fried and SD Conte, The plasma dispersion function. (Academic Press, New York, 1961)
70. C. Li *et. al.*, Measuring E and B Fields in laser-produced plasmas with monoenergetic proton radiography, Phys. Rev. Lett. **97**, 3 (2006)
71. FH Séguin *et. al.*, Spectrometry of charged particles from inertial-confinement-fusion plasmas. *Rev. Sci. Instrum.* **74**, 975 (2003)